Strojniški vestnik - Journal of Mechanical Engineering vol(yyyy)no, p-p
© 2018 Journal of Mechanical Engineering. All rights reserved.
DOI code
Original Scientific Paper
Received for review: yyyy-mm-dd
Received revised form: yyyy-mm-dd
Accepted for publication: yyyy-mm-dd

Comparative Experimental and Numerical Investigation on Electrical Discharge Drilling of AISI 304 using Circular and Elliptical Electrodes

Ali Tolga BOZDANA[1,*] - Nazar Kais AL-KHARKHI[2]
[1] Mechanical Engineering Department, University of Gaziantep, Turkey
[2] Automated Manufacturing Engineering, University of Baghdad, Iraq

This work introduces a new electrode geometry for making holes with high aspect ratio on AISI 304 using Electrical Discharge Drilling (EDD) process. In addition to commercially available cylindrical hollow electrode, elliptical electrode geometry has been designed, manufactured and implemented. The principal aim was to improve the removal of debris formed during erosion process that adversely affects aspect ratio, dimensional accuracy and surface integrity. The results were compared and discussed in order to evaluate the effectiveness of electrode geometry on machining performance of EDD process with respect to Material Removal Rate (MRR,) Electrode Wear Rate (EWR), and Tool Wear Ratio (TWR). Dimensional features and surface characteristics of drilled holes were also evaluated in aspects of Overcut (OC), Aspect Ratio (AR), and Surface Roughness (SR). The experimental results revealed that elliptical electrode is preferable for producing holes having good dimensional accuracy and improved surface quality. In addition, 3D models of flow field with liquid, gas, and solid phases are proposed for analyses of the interelectrode gap within machining zone. Based on the results obtained from models, elliptical electrode also exhibited good flushing capability for effective debris removal.

Keywords: electrical discharge drilling, stainless steel, electrode geometry, drilling performance, dimensional accuracy, surface quality

Highlights:

- New electrode with elliptical geometry was implemented for drilling of stainless steel using EDD process.
- A number of drilling operations were conducted using circular and elliptical electrodes to produce Ø3 mm holes.
- Effectiveness of both electrode geometries on drilling performance and hole characteristics was compared.
- 3D three-phase CFD models were developed to analyze flushing and debris removal at interelectrode gap.

0 INTRODUCTION

Stainless steel has been widely used in many fields of medical, defense, chemical, construction, and aerospace due to its characteristics of good corrosion resistance, low thermal conductivity and high strength at elevated temperatures [1]. Among other grades of stainless steels, AISI 304 SS is difficult to drill with conventional methods, and Electrical Discharge Drilling (EDD) process has been recently used for this purpose. EDD is an electro-thermal process used for drilling small holes on electrically conductive materials, which is based on the eroding effect of electric sparks occurring between tool electrode and workpiece [2]. Drilling operations are conducted by tubular (hollow) electrodes through which dielectric fluid is flowing for washing removed particles (debris) away from machining zone. Adequate flushing at interelectrode gap is of significant importance in drilling of holes with high aspect ratios. In such case, proper circulation of dielectric and effective debris removal are difficult to achieve, which affect drilling performance and hole features.

Numerous methods have been contrived in order to improve flushing in EDD applications. Some researchers have tried to manipulate the relative movement between electrode and workpiece to stimulate the debris removal. Orbital movement of tool electrode in radial direction was employed for manipulating side interelectrode gap [3, 4]. Bottom interelectrode gap was also manipulated by applying the ultrasonic vibrations in vertical direction [3, 5, 6]. Moreover, it is reported that increasing electrode rotation [7-9] and dielectric pressure [10-12] have provided improvements in

---

[*] Corr. Author's Address: Mechanical Engineering Department, University of Gaziantep, 27310, Gaziantep, Turkey, bozdana@gantep.edu.tr

flushing and drilling performance. On the other hand, only few studies were conducted for investigating the effect of electrode shape in EDD process. Nastasi and Koshy [13] added geometric features of helical and radial slots on cylindrical copper electrodes to improve the gap flushing in drilling of 6061 aluminum alloy. Plaza et al. [14] studied the effects of helix angle and flute depth on helical electrodes to improve debris removal while increasing the hole depth in drilling of Ti-6Al-4V. Another work on using helical electrode with implementation of ultrasonic vibrations on workpiece was conducted by Hung et al. [15] in drilling of nickel alloy Hymu 80.

Besides experimental works, there are few studies on modeling the flow characteristics at electrode-workpiece interaction. Nastasi and Koshy [13] modeled the flow fields in frontal and lateral gaps using ANSYS CFX to optimize the tool electrode comprising geometric features. Xie et al. [16] presented 2D flow model developed by CFD in ultrasonically assisted EDM process. Their model involved phases of kerosene dielectric and debris at bottom and side regions of interelectrode gap. Wang and Han [17, 18] proposed 3D model of flow field with liquid, gas, and solid phases to analyze the machining gap during electrode jump in EDM. The variations in bubble volume at interelectrode gap in ultrasonically assisted EDM were studied by Kong et al. [19]. 3D geometrical modeling of flow field at interelectrode gap was established using FLUENT software. In another study of Xie et al. [20], 2D model of flow field in ultrasonic assisted EDM was constructed with liquid and debris phases. Debris distribution and velocity variations at bottom and side gaps during ultrasonic vibration cycle were investigated. Zhang et al. [21] developed 2D model to simulate movement and distribution of debris in EDM with self-adaptive electrode movement. The results indicated that the quantity of debris flushed away was limited and most of debris in the gap was aggregated at interelectrode gap. It should be noted that there is no comprehensive work in related literature on modeling of flushing and debris removal in EDD process.

This study presents experimental and numerical investigations on drilling of stainless steel 304 using circular and elliptical electrodes. Several drilling operations were performed in order to examine the effectiveness of electrode geometry on machining performance as well as dimensional accuracy and surface quality of drilled holes. Numerical analyses were also carried out based on 3D three-phase CFD models for simulation of flushing capabilities of electrodes. The results were compared and discussed in detail.

1 METHODS and MEASUREMENTS

Tubular brass electrodes having two different geometries (Fig. 1) were used for drilling holes. Circular electrode is commercially available, and elliptical electrode was manufactured by forging of circular electrode. It was designed as such that both electrodes have the identical inner and outer diameters of Ø1 mm and Ø3 mm, respectively. It should be noted that the elliptical electrode has provided additional gap of 0.1 mm on each side. Thereby, elliptical electrode has the diameter of 2.8 mm on one side and 3 mm on the other side, resulting in drilling of holes having the same diameter as circular electrode.

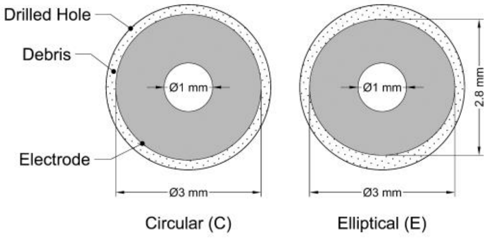

Fig. 1. Electrode geometries

Drilling operations were conducted on JS AD-20 EDD machine (Fig. 2). Vertical movement of tool electrode was achieved by servo control while axis movements were displayed on coordinate display. Machining settings were selected on control panel. Dielectric fluid was filtered and pumped through the hollow electrode throughout drilling process.

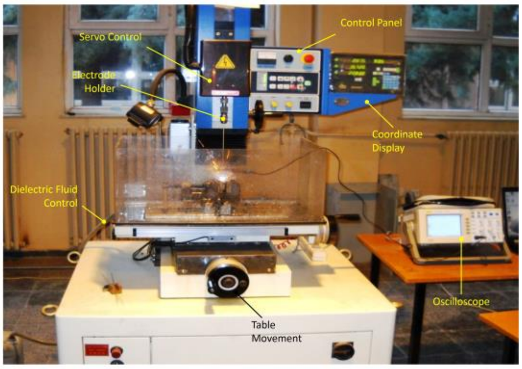

Fig. 2. EDD machine with experimental setup

Holes were drilled on specimens of AISI 304 (Fig. 3). They were produced on mating interface of specimens, and then separated after drilling to perform measurements on the hole surfaces.

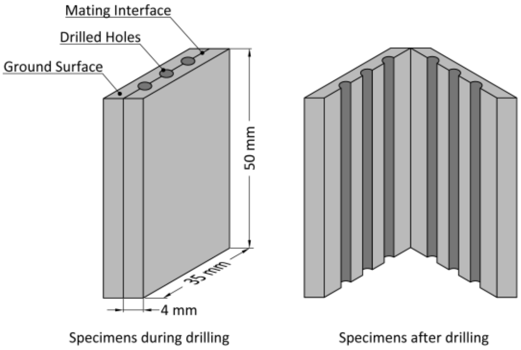

Fig. 3. Sketch of specimens

Table 1 presents the machining conditions. They were selected based on preliminary experiments. Five holes using both electrodes were drilled in durations of 1, 2, 3, 4, 5 min.

Table 1. Drilling parameters

Peak Current:	24 A
Pulse-on Time:	44 µs
Pulse-off Time:	5 µs
Voltage:	50 V
Capacitance:	1476 µF
Dielectric Fluid:	Deionized water
Dielectric Pumping Pressure:	50 kg/cm^2
Electrode Rotation Speed:	200 rpm

Process performance was evaluated by Material Removal Rate (MRR) and Electrode Wear Rate (EWR) as given in Eq. 1 and Eq. 2, respectively. Initial and final weights of specimens ($W_{s(i)}$ and $W_{s(f)}$) and electrode ($W_{e(i)}$ and $W_{e(f)}$) were weighed using a digital scale with precision of ±1 mg. Drilling time (t) was recorded by precision timer. Tool Wear Ratio (TWR) was also employed to evaluate the dimensionless relative effect between electrode wear and material removal (Eq. 3).

$$MRR\ (g/min) = \frac{(W_{s(i)}) - (W_{s(f)})}{t} \tag{1}$$

$$EWR\ (g/min) = \frac{(W_{e(i)}) - (W_{e(f)})}{t} \tag{2}$$

$$TWR = \frac{EWR}{MRR} \tag{3}$$

The dimensions of drilled holes were determined based on high-resolution photographs. Because of side-sparking between electrode and workpiece, the diameter of drilled hole (D_h) is always larger than the electrode diameter (D_e). This is called Overcut (OC), which was calculated based on enlargement in hole diameter with respect to electrode diameter (Eq. 4). Aspect Ratio (AR) of drilled holes was also considered as a measure of erosion capability of electrodes, as given in Eq. 5 where (H_h) refers to depth of drilled hole.

$$OC\ (\%) = \frac{D_h - D_e}{D_e} * 100 \tag{4}$$

$$AR = \frac{H_h}{D_h} \tag{5}$$

Surface quality of holes was evaluated based on Surface Roughness (SR). The roughness average (R_a) was measured on each hole surface using Mitutoyo SJ-401 roughness tester with a cut-off length of 0.8 mm. Measurements were repeated three times at different regions on each hole surface, and the average of readings was taken as the roughness value.

In addition, the surface topography of drilled holes was analyzed using micrographs taken by SEM Inspect S50. Micrographs were taken at the identical magnification and energy levels of 645X and 30 kV, respectively.

2 EXPERIMENTAL RESULTS and DISCUSSIONS

Fig. 4 shows the photographs of drilled holes using circular and elliptical electrodes at drilling times of 1, 2, 3, 4, 5 min. Table 2 presents the results of MRR, EWR, TWR, OC, AR, and SR after drilling operations.

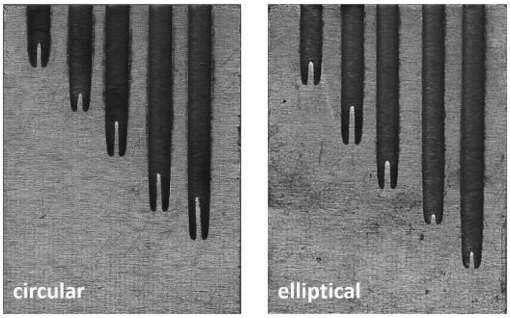

Fig. 4. Photographs of drilled holes

Table 2. Experimental results obtained by circular (C) and elliptical (E) electrodes

Hole	D_h (mm)		H_h (mm)		MRR (g/min)		EWR (g/min)		TWR		OC (%)		AR		SR (µm)	
No.	C	E	C	E	C	E	C	E	C	E	C	E	C	E	C	E
1	3.45	3.17	10.06	12.86	0.770	0.710	0.093	0.160	0.121	0.225	15.00	5.67	2.92	4.06	4.25	3.81
2	3.43	3.16	17.02	22.31	0.611	0.615	0.100	0.150	0.164	0.243	14.33	5.33	4.96	7.10	4.24	3.78
3	3.45	3.17	24.17	29.38	0.538	0.541	0.110	0.133	0.204	0.246	15.00	5.67	7.00	9.27	4.04	3.67
4	3.42	3.14	33.04	35.03	0.498	0.497	0.113	0.125	0.226	0.252	14.00	4.67	9.70	11.16	3.87	3.55
5	3.41	3.19	37.49	42.06	0.470	0.490	0.112	0.124	0.238	0.253	13.67	6.33	11.00	13.20	3.89	3.58

2.1 Drilling Performance

MRR is a significant output in EDD process due to its vital influence on the engineering economy. Higher MRR value refers to greater amount of material removal per unit time. The results of MRR for circular and elliptical electrodes are compared in Fig. 5. Elliptical electrode provides higher MRR as compared with circular electrode, resulting in deeper holes. This is due to the fact that the spark intensity was increased and flushing was improved in case of elliptical electrode. In other words, elliptical electrode promotes extra space for debris removal and flushing supply. Thus, greater amount of debris will flow away from interelectrode gap and higher MRR is obtained. It is also observed that MRR values for elliptical electrode are not diminished by certain hole depth whereas material removal with circular electrode becomes lesser with increasing the drilling depth. Moreover, MRR curves in Fig. 5 for both electrodes decrease with drilling depth since flushing the debris away from machining zone becomes more difficult.

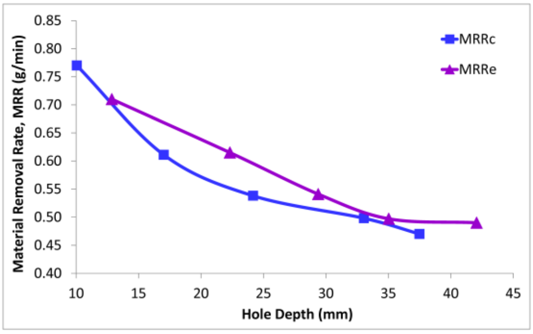

Fig. 5. MRR with respect to hole depth

EWR is also an important issue related with MRR. Fig. 6 shows EWR results for both electrodes. Elliptical electrode generally exhibits higher EWR, which is expected as the degree of erosion on both workpiece and electrode are proportional to each other. Thus, providing high MRR, elliptical electrode causes high EWR. However, EWR for elliptical electrode decreases with an increase in hole depth while EWR for circular electrode increases due to weak flushing. This causes accumulation of debris at machining zone, leading to increase in degree of erosion of electrode. Elliptical electrode has the advantage of providing its lowest degree of EWR, even in case of deep holes.

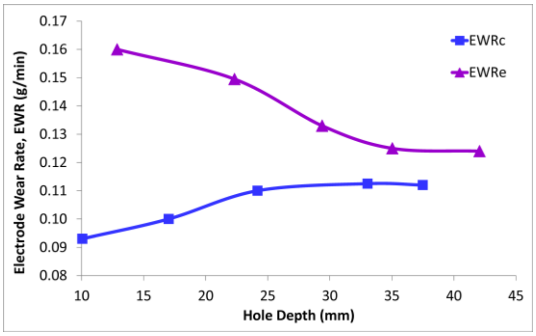

Fig. 6. EWR with respect to hole depth

TWR is employed to evaluate the combined effect of MRR and EWR. It is desirable to have lower TWR value since it refers to lesser amount of electrode wear and greater material removal. As seen in Fig. 7, moderate increase in TWR is observed for elliptical electrode whereas there is significant increase in case of circular electrode.

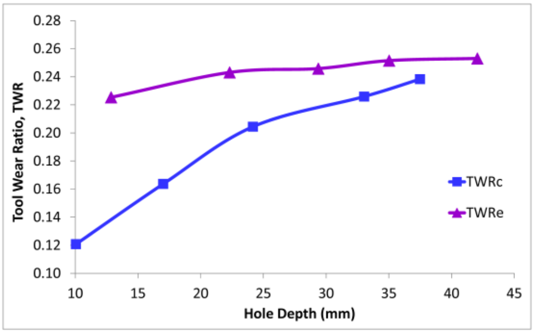

Fig. 7. TWR with respect to hole depth

2.2 Dimensional Accuracy

AR is mainly related with erosion capabilities of electrodes. MRR for each electrode geometry was different, and hence different drilling depths were obtained for each hole. The results in Fig. 8 reveal that elliptical electrode provided holes with higher AR, corresponding to greater amount of material removal within specified drilling time, and hence deeper holes were produced.

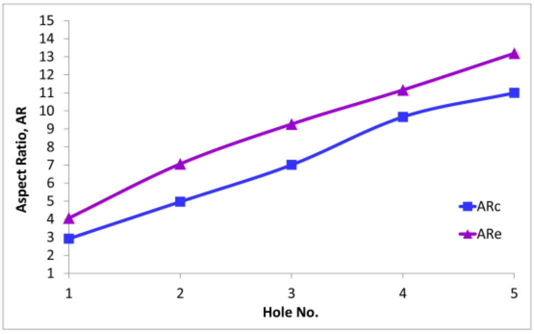

Fig. 8. AR with respect to hole number

Together with AR, OC is also an important issue in aspect of dimensional accuracy. Fig. 9 presents the results of OC. It is desirable that OC should be the minimum for producing accurate holes. As seen in Fig. 9, elliptical electrode exhibits lower OC for all holes. In case of circular electrode, sparks are generated along perimeter of electrode-workpiece gap. This leads to removal of material on the side-walls of drilled hole surface, causing enlargement in hole diameter. Moreover, amount of heat occurring in machining zone in case of elliptical electrode is less than that of circular electrode due to improved flow of dielectric fluid through the larger gaps, decreasing production of side-sparking and leading to lower OC.

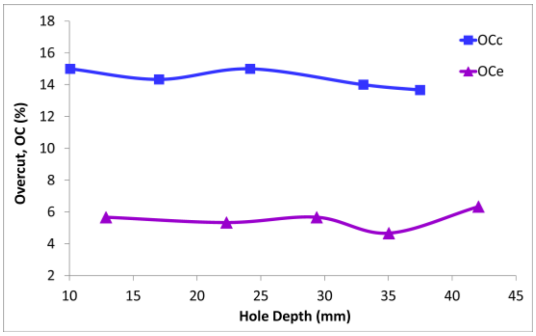

Fig. 9. OC with respect to hole depth

2.3 Surface Quality

The comparison for SR results is given in Fig. 10. Regardless of the hole depth, elliptical electrode provides smoother hole surfaces. This is owing to good flushing capabilities of elliptical electrode so that eroded particles can be effectively washed away without sticking on the workpiece surface, resulting in surfaces free from resolidified debris.

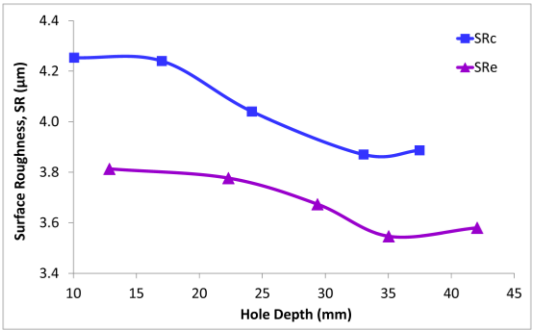

Fig. 10. SR with respect to hole depth

This conclusion is confirmed by means of surface topography of drilled hole surfaces (Fig. 11). In discharge drilling, sparking causes significant melting and vaporization of particles (i.e. debris). This debris solidifies when it comes in contact with dielectric fluid. Due to insufficient flushing, debris cannot be washed away and it sticks onto the workpiece surface. This leads to formation of surface anomalies (white layers and pockmarks), which adversely affect the surface quality. It is observed from Fig. 11 that the surface drilled by elliptical electrode provided less amount of white layer formation. This is due to improved flushing in case of elliptical electrode, and hence eroded particles were easily flushed away.

3 NUMERICAL ANALYSES

3.1 Theoretical Background

Flow characteristics were analyzed based on three-phase model of flushing (i.e. water as liquid phase, bubbles as gas phase, and debris as solid phase) in ANSYS FLUENT. The interaction between bubbles and water was simulated with Euler-Euler VOF model [16-18] by solving the volume continuity equation as follows [19]:

$$\frac{\partial y}{\partial t}(\alpha_g \rho_g) + \nabla.(\alpha_g \rho_g \upsilon_g) = \sum_{L=1}^{n}(m_{Lg}) \qquad (6)$$

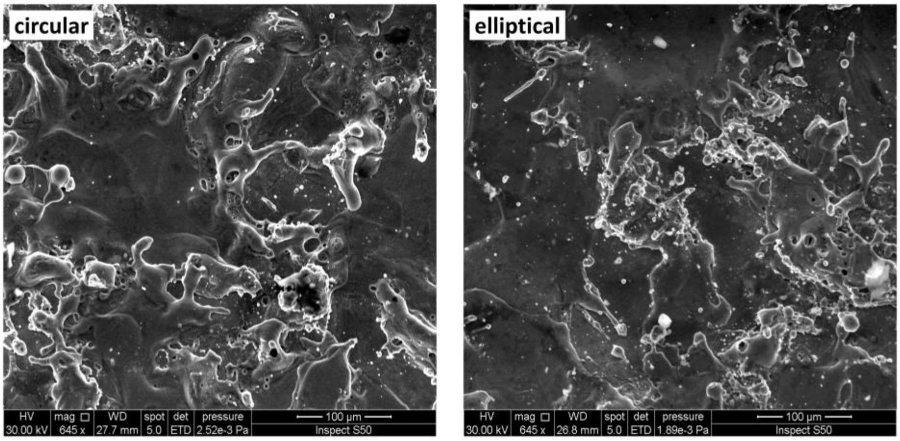

Fig. 11. SEM photographs of drilled surfaces

where α_g is the volume fraction of gas, ρ_g is the density of gas, υ_g is the velocity of gas, m_{Lg} is the mass transfer from liquid phase to gas phase. Function of DEFIEN_MASS_TRANSFER was used to describe the transfer of water into gas [17]. When discharge occurs, water starts being transferred into bubbles. Processing of the water volume fraction (α_w) was computed by the following equation [19]:

$$\alpha_g + \alpha_L = 1 \qquad (7)$$

For VOF model, single momentum conservation equation of the entire flow field was solved. The momentum equation was depending upon volume fractions of all phases through ρ and μ [17]:

$$\frac{\partial}{\partial t}(\rho_a \boldsymbol{v}) + \nabla.(\rho_a \boldsymbol{v}\boldsymbol{v}) = -\nabla p + \nabla.[\mu_a(\nabla \boldsymbol{v} + \nabla \boldsymbol{v}^{\mathrm{T}})] + \rho_a \mathbf{g} + \boldsymbol{F} \qquad (8)$$

where ρ_a and μ_a were taken as the average of volume fraction values of phases, and F denotes external body forces (i.e. forces from interaction with the dispersed phases). The calculations of ρ_a and μ_a for two phases are as follows:

$$\rho_a = \alpha_L \rho_L + \alpha_g \rho_g \qquad (9)$$

$$\mu_a = \alpha_L \mu_L + \alpha_g \mu_g \qquad (10)$$

where α_L and α_g are the volume fractions of liquid and gas phases, respectively.

Debris moves with dielectric fluid in machining gap, and hence their movement is abided by a discrete phase particle by integrating the force balance on debris, which is written in Lagrangian reference frame. The motion equation of debris in the gap flow can be determined by Newton's second law of motion [17]:

$$\frac{\mathrm{du_p}}{\mathrm{dt}} = \frac{\mathrm{g_z}(\rho_\mathrm{p}-\rho_\mathrm{L})}{\rho_\mathrm{p}} + \mathrm{F_z} + \mathrm{F_D}(\mathrm{u_L} - \mathrm{u_p}) \qquad (11)$$

where u_L and u_p are the velocities of water and debris in the direction of electrode movement, ρ_L and ρ_p are the densities of water and debris, g_z is the gravitational acceleration. The first term on the right side of Eq. 11 is the buoyancy of debris. The second term is an additional force (thermo-Phoresis force and brown force), including forces on particles arising due to rotation of reference frame. The third term is the drag force of debris, in which F_D was calculated as follows [17]:

$$F_D = \frac{18\mu}{\rho_p d_p^2}\frac{C_D R_e}{24} \qquad (12)$$

where μ is the molecular viscosity of fluid, d_p is the diameter of debris particles, R_e is Reynolds number, C_D is the coefficient of drag force.

The energy equation was also solved for VOF model as below [22]:

$$\frac{\partial}{\partial t}(\rho E) + \nabla.(\upsilon(\rho E + p)) = \nabla.(k_{\mathrm{eff}}\nabla T) + S_h \qquad (13)$$

VOF model treats energy (E) and temperature (T) as mass-averaged variables:

$$E = \frac{\sum_{q=1}^{n} \alpha_q \, \rho_q \, E_q}{\sum_{q=1}^{n} \alpha_q \, \rho_q} \qquad (14)$$

where E_q for each phase is based on the specific heat of that phase and the shared temperature. The properties of ρ and k_{eff} (effective thermal conductivity) are shared by phases. The source term (S_h) contains contributions from radiation as well as any other volumetric heat sources.

3.2 Construction of Models

3D models of flow field during consecutive-pulse discharge was created. The deionized water (i.e. liquid phase) was introduced through the inner portion of hollow electrode. The air (i.e. bubbles occurring due to vaporization) and the debris (i.e. particles eroded from workpiece) were generated within gap between electrode tip and workpiece. The model equations given in previous section were solved using a commercial CFD software package, FLUENT (v16.1).

CFD simulations were carried out by means of GAMBIT tools in order to design the problem in geometrical configuration with appropriate mesh. Before solving fluid flow problems, FLUENT needs the domain at which the flow takes place. Thereby, 3D flow domains for both electrode geometries were created in Solidworks®. After that, geometric model of flow field domain inside the electrode and within machining gap was divided into certain number of cells (intervals) using GAMBIT software, and then imported into FLUENT. Solid models and the corresponding meshing for both electrode geometries are shown in Fig. 12 and Fig. 13, respectively.

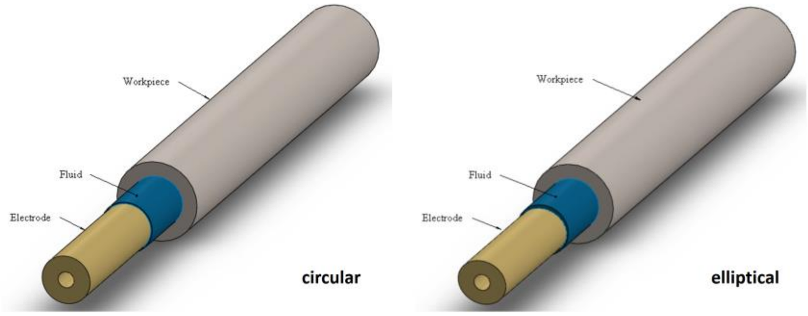

Fig. 12. Solid models representing electrode-fluid-workpiece interaction.

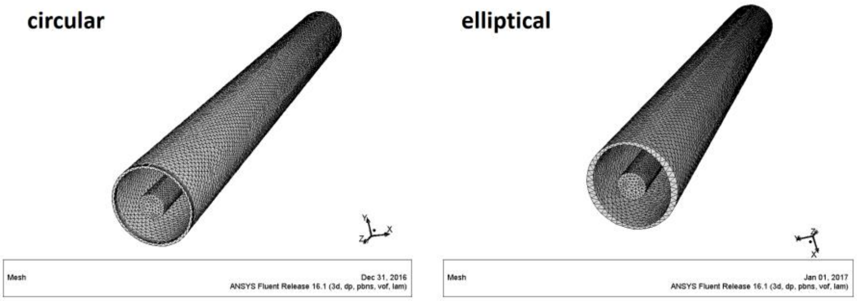

Fig. 13. Meshed models representing geometry at flushing gap

In order to obtain well-posed system of equations, reasonable boundary conditions for computational domain were implemented. The gap between electrode and workpiece was initially filled with liquid (i.e. deionized water). Air bubbles and debris started to occur at bottom region of electrode, resulting from the sparks generated at the tip of electrode, which melts the metal and boils the water. The outlet boundary condition was pressure that was set as $1.013{*}10^5$ Pa (i.e. atmospheric pressure). The pressure boundary condition was applied at top of electrode with static reference pressure of 50 kg/cm^2. The inlet velocity was calculated as:

$$\dot{m} = u_i \, A \qquad (15)$$

where $\dot{m}$ is the mass flow rate of water escaping from machining zone per unit time, A is the inside area of hollow electrode. The inlet velocity (u_i) was about 2 m/s. Wall boundary conditions were defined as no-slip condition for liquid whereas free-slip conditions for solid and gas phases. Side and bottom faces of electrodes were rotated at 200 rpm. The identical boundary conditions were applied for both electrode geometries.

Simulations were carried out using FLUENT software based on the setup, illustrated in Fig. 14. The maximum machining depth was 50 mm. Side and bottom gaps were measured as suggested in literature [18]. The difference between diameters of electrode and drilled hole was the dimension of side gap, and it was found to be about 100 µm. Dimension of bottom gap was determined based on the difference between vertical coordinates of electrode. The coordinate of electrode tip was recorded when spark occurred between electrode and workpiece. Without sparking, its coordinate was also recorded when electrode was in touch with workpiece. The difference between these two coordinates gives the dimension of bottom gap, which was found to be 480 µm.

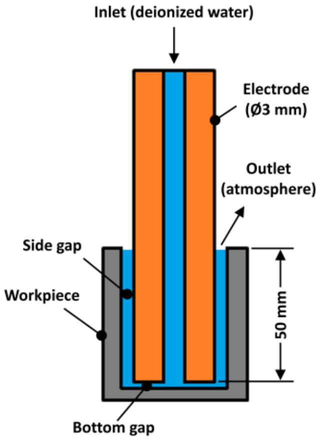

Fig. 14. Sketch of setup for numerical model

In order to verify the flow type of flow field in the machining gap (i.e. laminar or turbulent flow), Reynolds number (R_e) was calculated:

$$R_e = \frac{u\,L}{\nu} \qquad (16)$$

where u is the average speed of fluid flowing through the cross section of machining gap, L is the characteristic length of flow field, ν is the kinematic viscosity of water at machining gap.

For the side gap; the characteristic length was constant (0.1 mm), ν was considered as kinematic viscosity of water (i.e. $0.801{*}10^{-6}$ m^2/s), υ was considered as the speed of water at side gap as calculated above. Thus, the maximum Reynolds number of the side gap was calculated as 413. This value is much smaller than the critical value of 2300, and hence flow was said to be laminar.

In discrete phase model, debris was assumed to have spherical shape with diameter of 25 µm [17]. The phase properties are given in Table 3.

Table 3. Properties for phases

Property	*Liquid (water)*	*Solid (AISI 304)*	*Gas (air)*
Density (kg/m^3)	998.2	7000	1.225
Conductivity (W/m-°K)	0.6	17	0.0242
Specific Heat (J/kg-°K)	4182	530	1006.43
Viscosity (kg/m-s)	100.3 E-05	-	1.7894 E-05

3.3 Results and Discussions

Numerical simulations of inter-electrode gap were carried out to show the effectiveness of electrode shape on behavior of air bubbles and debris distribution at incremental time steps. Firstly, bubble distributions were simulated to define the motion of air bubbles from bottom gap to side gap. Fig. 15 shows the simulation results of volume fraction at increasing time steps of 0.001, 0.005, and 0.01 s. The left column of numerals with different color fringes correspond to the volume fraction of bubbles. For instance, the regions of blue color denoted by “0” are full of water. Results in Fig. 15 reveal that circular electrode exhibits uniformly distributed of areas of bubbles around side gap. On the other hand, the bubble distribution is nonuniform in case of elliptical electrode, owing to its elliptical shape. The regions within the sides of larger gap due to elliptical shape provides extra space for bubbles to flow, leading to stimulated motion of bubbles, which results in effective flushing capabilities.

Similar effects were observed for the debris distributions, as presented in Fig. 16. The left column of numerals with different color fringes correspond to the accumulated moving time of debris. Regardless of moving direction of debris and velocity field, the dispersion degree of debris in case of circular electrode is higher than that of elliptical electrode. It can be seen that flushing of debris was increased when elliptical electrode was used. Simulation results reveal that elliptical electrode has a significant influence on the debris exclusion from machining zone, and hence it has exhibited better flushing characteristics than circular electrode.

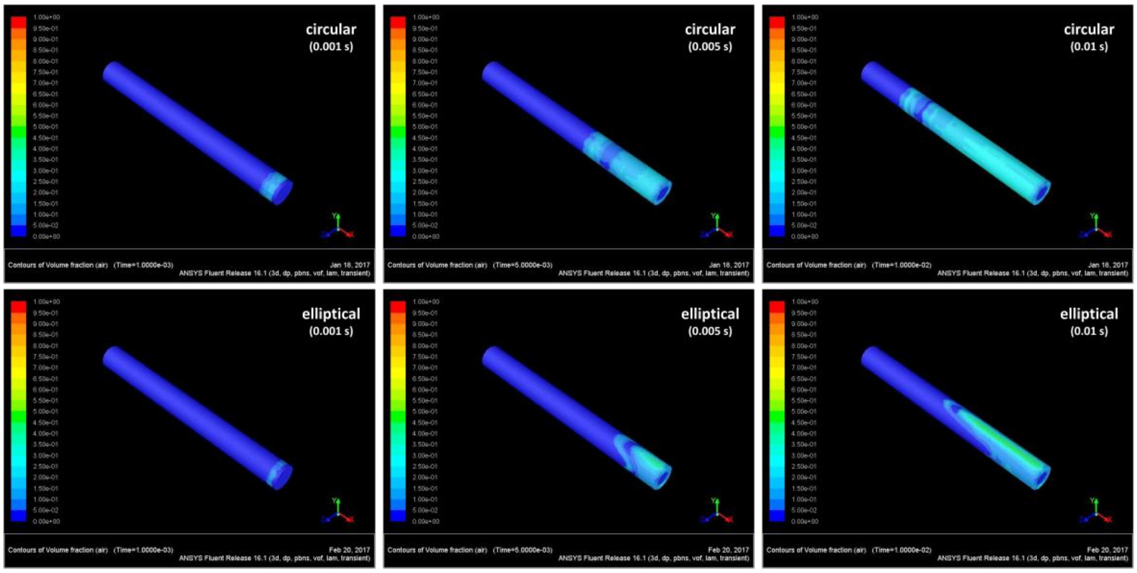

Fig. 15. Volume fraction contours of bubbles

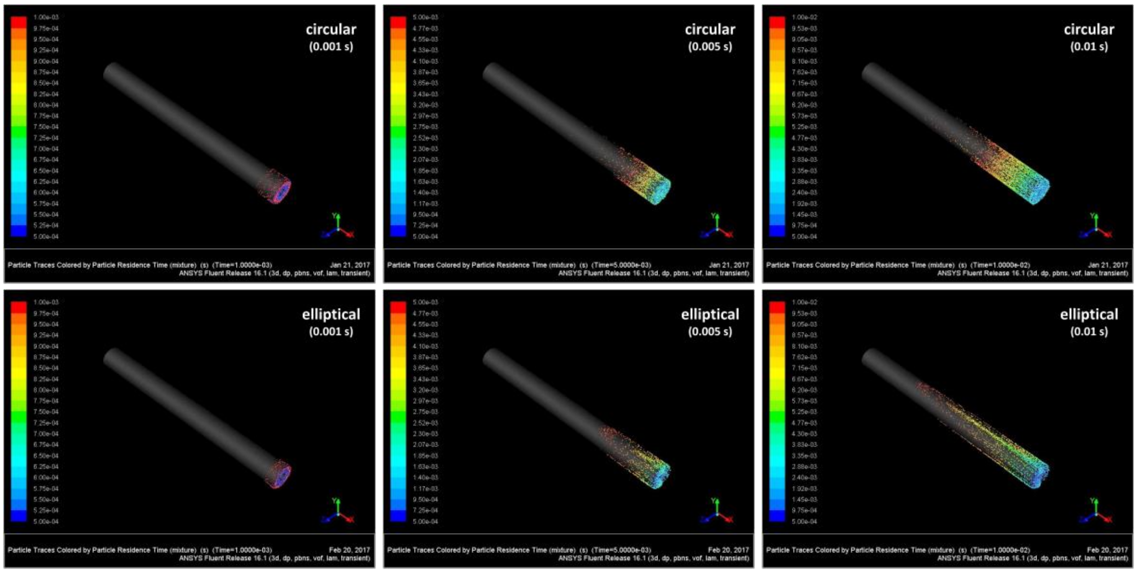

Fig. 16. Debris distributions

Debris concentrations along hole depth are shown in Fig. 17. It is revealed that elliptical electrode exhibits higher level of debris exclusion towards the outlet section of hole, which is far away from the bottom of hole (i.e. at the depth of 20 mm). On the other hand, in case of circular electrode, debris exclusion is diminished before 15 mm. This proves that elliptical electrode has good flushing capabilities for effective debris removal, even at deep hole regions.

The reliability of developed models was validated based on Mass Flow Rate (MFR). For this purpose, several tests were conducted at varying drilling depths (at a range of 1-50 mm) and inlet MFR values were measured. The corresponding outlet MFR values from models were compared with experimental values. Fig. 18 shows that there is good agreement between experimental and numerical MFR values. CFD model has provided a linear correlation with high coefficient of determination (i.e. R^2 = 0.969). This assures the reliability of developed model for accurate simulation of flow field at interelectrode gap.

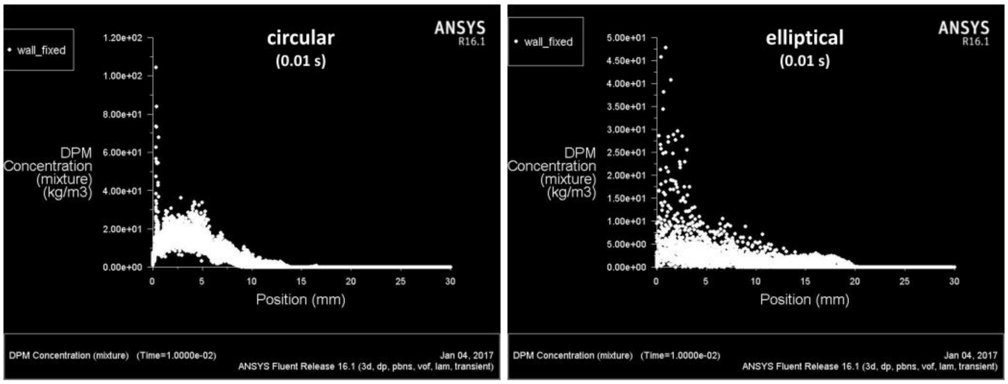

Fig. 17. Discrete phase models for debris concentration along the hole depth

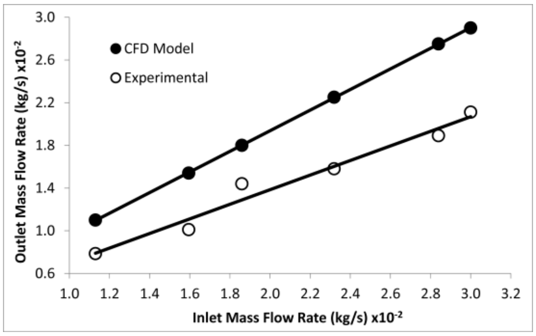

Fig. 18. Validation of MFR

4 CONCLUSIONS

In this research, circular and elliptical hollow electrodes were used in drilling of Ø3 mm holes on AISI 304 using EDD process. Several drilling operations were conducted at varying durations. Numerical models were developed for analysis of flushing capabilities. Both experimental and numerical results revealed that electrode shape has significant effects on machining performance as well as dimensional and surface characteristics of drilled holes.

The main outcomes of this study are as follows:

- In aspect of machining performance, elliptical electrode provided greater MRR and EWR as compared to circular electrode. Similar results were observed for TWR. The modifications on electrode shape affected erosion characteristics of workpiece and electrode, leading to changes in material removal and electrode wear.
- In assessment of dimensional features, holes with higher aspect ratio (i.e. deeper holes) were obtained by elliptical electrode. Owing to its elliptical shape, spark intensity was increased at the bottom interelectrode gap, causing greater amount of material removal (i.e. deeper holes). Elliptical electrode also provided holes with lower OC. This is because of narrower contour along perimeter of elliptical electrode, leading to less amount of side-sparking, resulting in smaller enlargement on hole diameter.
- Regarding the surface quality of drilled holes, elliptical electrode provided lower SR values. It has better flushing performance due to the extra space at the side interelectrode gap, allowing for easier removal of debris so that smoother hole surfaces were obtained.
- The numerical results based on 3D three-phase models also proved that elliptical electrode has good flushing capabilities for efficient removal of air bubbles and eroded particles.

In spite of high electrode wear, the overall performance of elliptical electrode over circular electrode was superior due to improved erosion and flushing capabilities. Elliptical electrode had provided holes with higher aspect ratio (up to 42%), less overcut (down to 66%), and lower surface roughness (down to 7%). It is revealed that elliptical electrode is preferable for producing deep holes with good dimensional accuracy and high surface quality.

REFERENCES

[1] Sarikaya, M., Yilmaz, V. (2016). Optimization and predictive modeling using S/N, RSM, RA and ANNs for micro-electrical discharge drilling of AISI 304 stainless steel. *Neural Computing and Applications*, p. 1-15, DOI:10.1007/s00521-016-2775-9 2.

[2] Bozdana, A.T., Ulutas, T. (2016). The effectiveness of multi-channel electrodes on drilling blind holes on Inconel 718 by EDM process. *Materials and Manufacturing Processes*, vol. 31, p. 504-513, DOI:10.1080/10426914.2015.1059451.

[3] Yu, Z.Y., Rajurkar, K.P., Shen, H. (2009). High aspect ratio micro-hole drilling aided with ultrasonic vibration and planetary movement of electrode by micro-EDM. *Annals of CIRP: Manufacturing Technology*, vol. 58, no. 1, p. 213-216, DOI:10.1016/j.cirp.2009.03.111.

[4] Bamberg, E., Heamawatanachai, S. (2009). Orbital electrode actuation to improve efficiency of drilling micro-holes by micro-EDM. *Journal of Materials Processing Technology*, vol. 209, no. 4, p. 1826-1834, DOI:10.1016/j.jmatprotec.2008.04.044.

[5] Jahan, M.P., Wong, Y.S., Rahman, M. (2012). Evaluation of the effectiveness of low frequency workpiece vibration in deep-hole micro-EDM drilling of tungsten carbide. *Journal of Manufacturing Processes*, vol. 14, no. 3, p. 343-359, DOI:10.1016/j.jmapro.2012.07.001.

[6] Shabgard, M.R., Alenabi, H. (2015). Ultrasonic assisted electrical discharge machining of Ti-6Al-4V alloy. *Materials and Manufacturing Processes*, vol. 30, no. 8, p. 991-1000, DOI:10.1080/10426914.2015.1004686.

[7] Yahagi, Y., Koyano, T., Kunieda, M., Yang, X. (2012). Micro drilling EDM with high rotation speed of tool electrode using the electrostatic induction feeding method. *Procedia CIRP*, vol. 1, p. 162-165, DOI:10.1016/j.procir.2012.04.028.

[8] Yadav, U.S., Yadava, V. (2015). Experimental investigation on electrical discharge drilling of Ti-6Al-4V alloy. *Machining Science and Technology*, vol. 19, no. 4, p. 515-535, DOI:10.1080/10910344.2015.1085316.

[9] Dwivedi, A.P., Choudhury, S.K. (2016). Effect of tool rotation on MRR, TWR, and surface integrity of AISI-D3 steel using the rotary EDM process. *Materials and Manufacturing Processes*, vol. 31, no. 14, p. 1844-1852, DOI:10.1080/10426914.2016.1140198.

[10] Munz, M., Risto, M., Haas, R. (2013). Specifics of flushing in electrical discharge drilling. *Procedia CIRP*, vol. 6, p. 83-88, DOI:10.1016/j.procir.2013.03.024.

[11] Selvarajan, L., Narayanan, C.S., Jeyapaul, R. (2015). Optimization of process parameters to improve form and orientation tolerances in EDM of MoSi2-SiC composites. *Materials and Manufacturing Processes*, vol. 30, no. 8, p. 954-960, DOI:10.1080/10426914.2014.962041.

[12] Selvarajan, L., Narayanan, C.S., Jeyapaul, R. (2016). Optimization of EDM parameters on machining Si3N4-TiN composite for improving circularity, cylindricity, and perpendicularity. *Materials and Manufacturing Processes*, vol. 31, no. 4, p. 405-412, DOI:10.1080/10426914.2015.1058947.

[13] Nastasi, R., Koshy, P. (2014). Analysis and performance of slotted tools in electrical discharge drilling. *Annals of CIRP: Manufacturing Technology*, vol. 63, no. 1, p. 205-208, DOI:10.1016/j.cirp.2014.03.054.

[14] Plaza, S., Sanchez, J.A., Perez, E., Gil, R., Izquierdo, B., Ortega, N., Pombo, I. (2014). Experimental study on micro EDM-drilling of Ti6Al4V using helical electrode. *Precision Engineering*, vol. 38, no. 4, p. 821-827, DOI:10.1016/j.precisioneng.2014.04.010.

[15] Hung, J.C., Lin, J.K., Yan, B.H., Liu, H.S., Ho, P.H. (2006). Using a helical micro-tool in micro-EDM combined with ultrasonic vibration for micro-hole machining. *Journal of Micromechanics and Microengineering*, vol. 16, no. 12, p. 2705-2713, DOI:10.1088/0960-1317/16/12/025.

[16] Xie, B., Zhang, Y., Zhang, J., Rend, S. (2015). Numerical study of debris distribution in ultrasonic assisted EDM of hole array under different amplitude and frequency. *International Journal of Hybrid Information Technology*, vol. 8, no. 5, p. 151-158, DOI:10.14257/ijhit.2015.8.5.17.

[17] Wang, J., Han, F. (2014). Simulation model of debris and bubble movement in consecutive-pulse discharge of electrical discharge machining. International *Journal of Machine Tools and Manufacture*, vol. 77, p. 56-65, DOI:10.1016/j.ijmachtools.2013.10.007.

[18] Wang, J., Han, F. (2014). Simulation model of debris and bubble movement in electrode jump of electrical discharge machining. *International Journal of Advanced Manufacturing Technology*, vol. 74, no. 5-8, p. 591–598, DOI:10.1007/s00170-014-6008-z.

[19] Kong, W., Guo, C., Zhu, X. (2015). Simulation analysis of bubble motion under ultrasonic assisted electrical discharge machining. *3rd International Conference on Machinery, Materials and Information Technology Applications (ICMMITA)*, Atlantis Press, DOI:10.2991/icmmita-15.2015.320.

[20] Xie, B., Zhang, Y., Zhang, J., Dai, Y., Liu, X. (2015). Flow field simulation and experimental investigation of ultrasonic vibration assisted EDM holes array. *International Journal of Control and Automation*, vol. 8, no. 12, p. 419-424, DOI:10.14257/ijca.2015.8.12.38.

[21] Zhang, W., Liu, Y., Zhang, S., Ma, F., Wang, P., Yan, C. (2015). Research on the gap flow simulation of debris removal process for small hole EDM machining with Ti alloy. *4th International Conference on Mechatronics, Materials, Chemistry and Computer Engineering (ICMMCCE)*, Atlantis Press, DOI:10.2991/icmmcce-15.2015.409.

[22] *ANSYS FLUENT 12.0 (Theory Guide)*. Ansys Inc. (2009).